High-Density Optical Coherence Tomography Analysis Provides Insights Into Early/Intermediate Age-Related Macular Degeneration Retinal Layer Changes

Matt Trinh,[1,2] Michael Kalloniatis,[1,2] David Alonso-Caneiro,[3] and Lisa Nivison-Smith[1,2]

[1]Centre for Eye Health, University of New South Wales, Sydney, New South Wales, Australia
[2]School of Optometry and Vision Science, University of New South Wales, Sydney, New South Wales, Australia
[3]Contact Lens and Visual Optics Laboratory, Queensland University of Technology, Brisbane, Queensland, Australia

Correspondence: Lisa Nivison-Smith, School of Optometry and Vision Science, University of New South Wales, Sydney, NSW 2052, Australia; l.nivison-smith@unsw.edu.au.

Received: January 28, 2022
Accepted: May 10, 2022
Published: May 27, 2022

Citation: Trinh M, Kalloniatis M, Alonso-Caneiro D, Nivison-Smith L. High-density optical coherence tomography analysis provides insights into early/intermediate age-related macular degeneration retinal layer changes. *Invest Ophthalmol Vis Sci.* 2022;63(5):36. https://doi.org/10.1167/iovs.63.5.36

Purpose. To topographically map all of the thickness differences in individual retinal layers between early/intermediate age-related macular degeneration (AMD_{early}/AMD_{int}) and normal eyes and to determine interlayer relationships.

Methods. Ninety-six AMD_{total} (48 AMD_{early} and 48 AMD_{int}) and 96 normal eyes from 192 participants were propensity-score matched by age, sex, and refraction. Retrospective optical coherence tomography (OCT) macular cube scans were acquired, and high-density (60 × 60 0.01-mm^2) grid thicknesses were custom extracted for comparison between AMD_{total} and normal eyes corrected for confounding. Resultant "normal differences" underwent cluster, interlayer correlation, and dose–response analyses for the retinal nerve fiber layer (RNFL), ganglion cell layer (GCL), inner plexiform layer (IPL), inner nuclear layer (INL), outer plexiform layer (OPL), outer nuclear layer + Henle's fiber layer (ONL_{+HFL}), inner and outer segment (IS/OS) thickness, and retinal pigment epithelium (RPE) to Bruch's membrane (BM) thickness.

Results. AMD_{total} inner retinal clusters demonstrated extensively thinned RNFL, GCL, IPL, and paracentral INL and thickened INL elsewhere, with normal difference means ranging from −8.13 µm (95% confidence interval [CI], −11.12 to −5.13) to 1.58 µm (95% CI, 1.07–2.09) ($P < 0.0001$ to $P < 0.05$). Outer retinal clusters displayed thinned paracentral OPL/ONL_{+HFL}, central IS/OS, and peripheral RPE–BM and thickened central RPE–BM, with means ranging from −1.31 µm (95% CI, −2.06 to −0.55) to 2.99 µm (95% CI, 0.97–5.01] ($P < 0.0001$ to $P < 0.05$). Effect sizes (−2.56 to 9.93 SD), cluster sizes, and eccentricity effects varied. All interlayer correlations were negligible to moderate regardless of AMD severity. Only the RPE–BM was partly thicker with greater AMD severity (up to 5.44 µm; 95% CI, 4.88–6.00; $P < 0.01$).

Conclusions. From the early stage, AMD eyes demonstrate thickness differences compared to normal with unique topographies across all retinal layers. Poor interlayer correlations highlight that the outer retina inadequately reflects complete retinal health. The clinical importance of OCT assessment across all individual retinal layers in early/intermediate AMD requires further investigation.

Keywords: age-related macular degeneration, anatomy, clustering, optical coherence tomography, spatial, topography, retinal thickness

The outer retina has typically been considered the fundamental site of insult in age-related macular degeneration (AMD).[1,2] Compounding evidence has demonstrated that in vivo alterations also occur within inner retinal layers in the early stages of AMD.[3–10] The interlayer relationships are unknown, although various pathophysiological models suggest that outer retinal degeneration may link to inner retinal changes via some cause-and-effect mechanisms.[11,12] Understanding the topography of anatomical differences between AMD and normal eyes and their interlayer relationships could have significant clinical implications, such as identifying where clinicians should be looking for change and answering whether patients with early or intermediate AMD could benefit from complete retinal optical coherence tomography (OCT) evaluation rather than solely focusing on the outer retina.

Previous topographical analyses of the retina have been defined using the Early Treatment for Diabetic Retinopathy Study (ETDRS) spatial template. These analyses, however, are low density, confining retinal space to nine unequal units (0.79- to 3.36-mm^2 areal sectors),[3–5] which hinders effective topographical interpretation within and between layers. For example, assessing the effect of eccentricity on retinal layer thicknesses using the ETDRS sectors limits eccentricity to three unequally sized sectors (central, inner, and outer) and assumes perfect concentricity and symmetry, thus

inducing the modifiable areal unit problem (MAUP)—statistical bias based on how data are spatially grouped.[13,14] Similarly, comparing retinal thickness differences between layers using the large ETDRS sectors disallows minute adjustments for displacements of Henle's fibers.[15]

We recently addressed these problems by defining retinal space according to 64 equal units (8 × 8 0.74-mm^2 areal grids).[16–21] This moderate-density analysis revealed that normal macular gridwise thicknesses could be assigned to spatial groups of statistically similar within-group data and statistically separable between-group data (i.e., clusters, representative of normal macular anatomical topography and less variable than ETDRS sectors).[19] Comparing intermediate AMD to normal eyes using moderate-density analysis revealed extensive topographical differences and potential interlayer relationships across most retinal layers[16,17] that had not been observed in previous ETDRS-based analyses, underlining the benefit of greater spatial (lateral) resolution for OCT thickness analysis.

There remained some unresolved questions associated with moderate-density analysis.[17] First, topographical patterns of thickness differences were equivocal in the retinal nerve fiber (RNFL) and inner nuclear layer (INL) and at the fovea of inner retinal layers. Correlations were also weak across most interlayer comparisons. It was not clear whether these were true anatomical outcomes or a consequence of incomplete resolution of the MAUP, as clustering was applied prior to comparisons between AMD and normal eyes and therefore assumed topographical differences followed normal macular anatomy. Second, grid size was still spatially coarse relative to the micrometer scale of macular cellular densities.[22–26] Hence, moderate-density analysis may have been incapable of depicting steep gradients of thicknesses and adjusting for lateral displacements of Henle's fibers between the outer and inner retina which range from 0.13 to 0.64 mm.[15]

Recently, we developed a high-density approach that defines retinal space according to 3600 equal units (60 × 60 0.01-mm^2 areal grids).[27] Greater lateral resolution enables spatially refined topographical interpretation (otherwise masked by lower resolutions) that appropriately represents steep gradients of thicknesses and allows minute adjustments for displacements of Henle's fibers. Modified cluster application after thickness comparisons between AMD and normal eyes will also resolve the MAUP by not making a priori model assumptions about macular topography; instead, clustered thickness differences will represent topographical maps of changes that may occur between AMD and normal eyes. Therefore, we hypothesize that OCT high-density analysis of early/intermediate AMD compared to normal eyes will enable topographical mapping of thickness differences in all individual retinal layers and clarify whether these interlayer differences are related. This could help guide future clinical assessments for the early stages of AMD by identifying where changes may occur and whether OCT evaluation of the outer retina alone can sufficiently depict complete retinal integrity.

Methods

Study Population

The study population was recruited through retrospective review of patient records from the Centre for Eye Health (CFEH), Sydney, Australia, from July 12, 2010, to February 20, 2021. CFEH is a referral-based clinic providing advanced diagnostic testing and management of ocular disease by optometrists and ophthalmologists.[28] All participants in this study had provided prior written informed consent for research use of their de-identified data in accordance with the tenets of the Declaration of Helsinki, and the study was approved by the Biomedical Human Research Ethics Advisory Panel of the University of New South Wales.

To cover the breadth of AMD in its early stages, both AMD_{early} and AMD_{int} eyes were included and formed the AMD_{total} group. Eligibility of AMD_{total} eyes was based on the following criteria: age of ≥ 50 years, clinical diagnosis of AMD_{early} or AMD_{int},[29] and no other macular-involving disease or significant structural abnormalities such as vitreomacular traction, or intra-/subretinal deposits, fluid, pigment, or vascular changes. Clinical diagnosis of AMD was based on fundus photography between two or more non-blind investigators according to a modified Beckman Initiative classification.[29] Participants 50 to 54 years of age were considered to have AMD if all phenotypic criteria were fulfilled, consistent with other notable studies.[30–33] Phenotypic severity criteria for AMD were

- AMD_{early}—presence of medium drusen (≥63 to <125 µm) without pigmentary abnormalities related to AMD
- AMD_{int}—presence of large drusen (≥125 µm) or pigmentary abnormalities related to AMD with at least medium drusen

Eyes with any other macular-involving disease or significant structural abnormalities, reticular pseudodrusen, and/or any signs of late AMD (macular neovascularization, geographic atrophy, or disciform scarring) were excluded from the study.

Eligibility of normal eyes was based on the following criteria: age of ≥50 years, visual acuity better than 0.1 logMAR (20/25 Snellen) for participants <60 years old or 0.2 logMAR (20/32 Snellen) for participants ≥60 years old, intraocular pressure <22 mmHg in both eyes, and no macular-involving disease or significant structural abnormalities as described above. One eye was selected per participant, and where both eyes were eligible simple randomization was used to select a random eye.

Propensity-Score Matching

Propensity-score matching, using multivariable logistic regression based on age, sex, and spherical equivalent refraction, was applied first to AMD_{early} and AMD_{int} eyes with an equal number of participants per group. AMD_{total} eyes were then propensity-score matched to an equal number of normal eyes. Fuzzy matching without replacement of propensity scores was performed to randomize the selection of participants and reduce an imbalance of potentially confounding co-variables between groups, hence mitigating selection bias,[34,35] rather than exact matching, which leaves individuals unmatched in a limited sample pool. Match tolerance was increased after each iterative random draw until the maximum number of matches. This resulted in relatively balanced propensity scores among groups (logistic regression predicted probability mean ± SD for AMD_{early}, 0.49 ± 0.1; AMD_{int}, 0.51 ± 0.07; AMD_{total}, 0.52 ± 0.16; normal, 0.43 ± 0.17).[36]

Image Acquisition and Retinal Layer Segmentation

OCT macular cube scans comprised of 61 B-scans spaced 120 µm apart within an area of 8600 × 7167 µm or 30° × 25° were obtained using the SPECTRALIS SD-OCT (Heidelberg Engineering, Heidelberg, Germany). This scanning protocol contained the highest number of B-scans using commercially available SPECTRALIS SD-OCT settings without significantly compromising image quality.[37] If multiple scans were available per participant, the earliest scan meeting the inclusion criteria, above 15-dB signal strength, and without significant artifacts was used. Ocular tilt, automatic segmentation, and manual correction were applied to each scan via the HRA/SPECTRALIS Viewing Module 6.9.5.0 (Heidelberg Engineering).

Participants were randomized into one of two blocks, and each block was assigned to an optometrist (MT or VK) for independent review and manual correction of segmentation where necessary for the RNFL, ganglion cell layer (GCL), inner plexiform layer (IPL), INL, outer plexiform layer (OPL), outer nuclear layer + Henle's fiber layer (ONL_{+HFL}), inner and outer segment (IS/OS) thickness, and retinal pigment epithelium to Bruch's membrane (RPE–BM) thickness (Fig. 1A, brown insert). The optometrists then reviewed the alternate block, and any further manual correction was resolved through discussion and consensus between them. Consensus for all segmentation was reached after one session of discussion. Blinding of graders to participant disease status during outer retinal segmentation was not possible, as drusen and/or pigmentary changes are obvious, and masking of the outer retina during inner retinal segmentation is yet unavailable in commercial OCT software. Although this may have produced potential bias, manual correction of segmentation has shown excellent repeatability and reproducibility in AMD eyes[38] and therefore was regarded as the ground truth for retinal anatomy (as opposed to automatic segmentation) in concordance with other studies.[39–41] Notably, segmentation boundaries were manually corrected to continue through large vasculature to mitigate their effect on thicknesses (Fig. 1A, magenta insert, asterisk). Segmentation was also corrected to combine Henle's fiber layer with the ONL as commonly done in OCT studies due to its inconsistent reflectivity (although anatomically part of the OPL) (Fig. 1A, cyan insert, arrowhead), and to resolve mis-segmentation around drusen (Fig. 1A, cyan insert, dagger).

High-Density Grid Data Extraction

Thicknesses were custom extracted across 3600 grids (60 × 60 0.01-mm^2 areal units; 115 × 115 µm or 0.4° × 0.4° sided units) centered on the fovea and totaling an area of 6880 × 6880 µm or 24° × 24° (Fig. 1B). The grid density (i.e., 60 × 60 grids) was selected to maximize coverage of segmented thickness values within the 61 total B-scans of each macular cube. Therefore, each grid contained approximately one B-scan. The automatic real time (i.e., number of image frames averaged per location) was increased from the default nine to 12 to improve the signal-to-noise ratio.[37] The total grid area (i.e., 6880 × 6880 µm) was selected because it was commensurate with the commercially available SPECTRALIS SD-OCT total grid area using 64 grids (8 × 8 0.74-mm^2 areal units) as seen in previous studies.[16,17,19] Note that the total grid area did not cover the entire macular cube scan of 8600 × 7167 µm or 30° × 25°. Custom extraction was performed using code developed in MATLAB 9.9 (MathWorks, Natick, MA, USA) by author DAC. Grids that were completely covered by a retinal blood vessel, distinct peripapillary atrophy, or the optic nerve were manually excluded to minimize potential confounding. Exclusion of these grids was applied to all retinal layers for each participant to mitigate any related potential confounding (e.g., shadowing) (Fig. 1A, yellow insert).

Corrected Thickness Comparisons

Grid-wise thicknesses for normal eyes were corrected for age, sex, and refraction using the multivariable linear regression model:

$$y_n = ax_1 + bx_2 + cx_3 + k$$

where y = corrected thickness (µm); n = grid number from 1 to 3600; x_1 = age (years); x_2 = sex (binary; males = 0, females = 1); x_3 = refraction (spherical equivalent diopters [D]); a, b, and c are coefficients; and k is a constant.

Refraction was used as a surrogate for axial length, as previous systematic review has demonstrated strong correlation between the two variables.[42] Gridwise thicknesses were then compared between AMD_{total} and corrected normal eyes, and the resultant values were denoted as gridwise normal differences:

$$z_n = \left(\mathrm{AMD}_{\mathrm{total}}\mathrm{grid}_n\mathrm{thickness}\right) - y_n$$

where z = normal difference (µm). For example, $grid_n$ of an AMD eye from a 57-year-old female with −3.00 D refraction would be compared to $grid_n$ of a normal eye corrected to the equivalent of a 57-year-old female with −3.00 D refraction. The rigorous use of corrected thickness for each of the 3600 grids for each retinal layer for each participant was implemented to ensure that gridwise comparisons were not confounded by multiple variables. Correction was applied at the gridwise level (pre-clustering), instead of at the group level (post-clustering) as performed in previous work,[16,17] so as not to assume that all grids within each spatial group (cluster) shared exactly the same regression characteristics. This was done to address the MAUP, which states that statistical bias may be introduced based on how data are spatially grouped.[13,14]

Cluster Analysis

Unsupervised cluster analysis was performed to identify new spatial groupings of retinal thickness changes between AMD_{total} and normal eyes (i.e., normal differences). Groupings were comprised of normal differences that were statistically similar within clusters and statistically separable between clusters.[43] AMD_{early} and AMD_{int} were set as independent groups, enabling further quantitative comparison between study groups.

Cluster number and size were not predefined to avoid violating statistical separability of cluster means and also inducing the MAUP[13,14] via a priori assumption that spatial patterns of change were uniform across all retinal layers despite their varying thickness distributions.[44] Instead, two-step clustering was selected for its proven robustness against many other cluster algorithms[45] and was applied to random

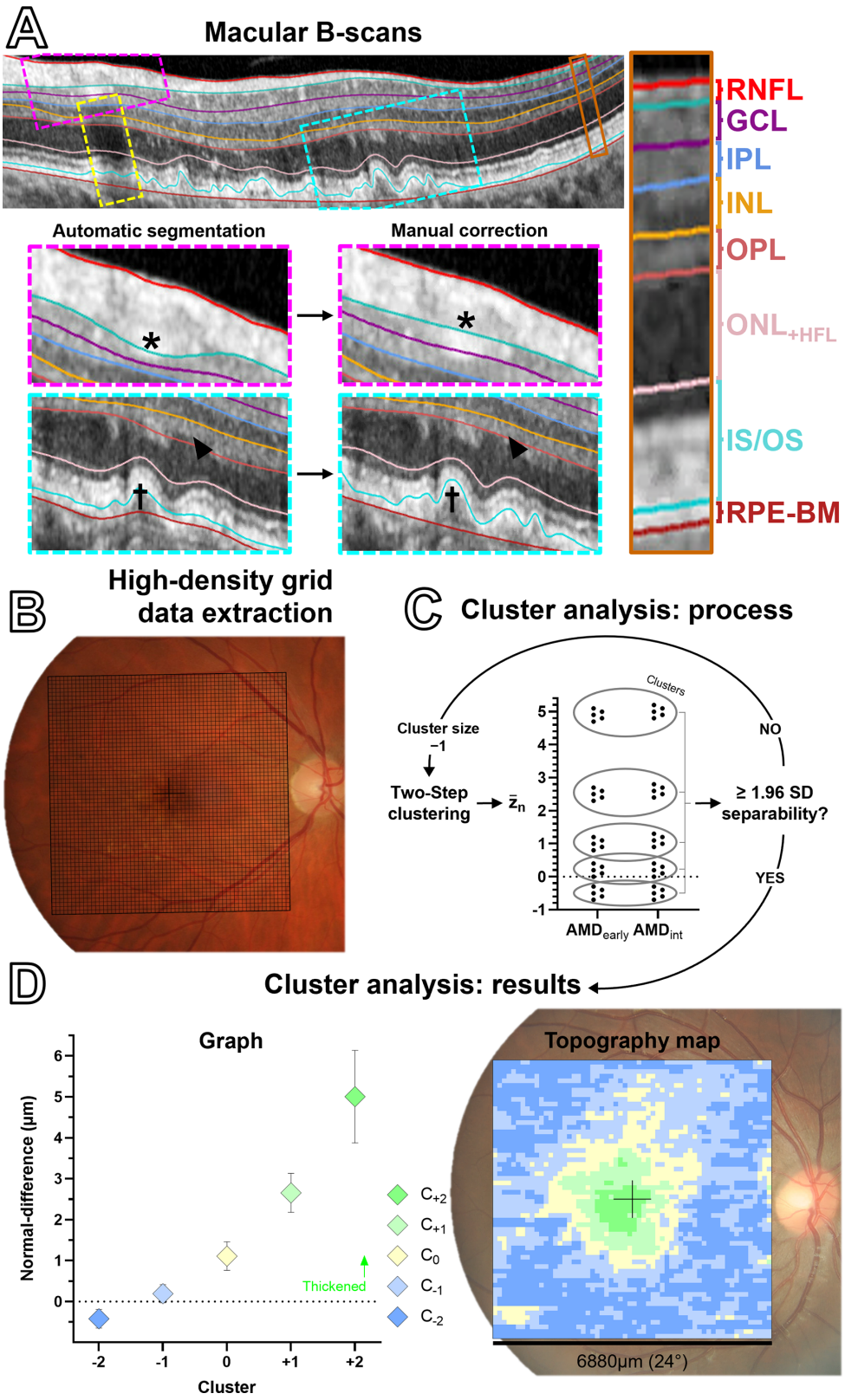

Figure 1. Macular volume scans within the SPECTRALIS HRA+OCT Viewing Module were automatically segmented and manually corrected to define the retinal layers in each B-scan (**A**).[17] Note that automatic segmentation boundaries were manually corrected to continue through large vasculature (*magenta insert*, *asterisk*), combine Henle's fiber layer with the ONL (*cyan insert*, *arrowhead*), and resolve mis-segmentation around drusen (*cyan insert*, *dagger*). Grids that were completely covered, such as by retinal blood vessel shadowing (*yellow*), were manually excluded. Thicknesses were extracted across 3600 (60 × 60) grids (total 6880 × 6880 µm or 24° × 24° area) centered on the fovea for each retinal layer (**B**). Gridwise thicknesses were compared between AMD_{total} and corrected normal eyes, and resultant values were denoted as normal differences (µm) = z_n, where n = grid number from 1 to 3600 in random order. Two-step clustering was performed with AMD_{early} and AMD_{int} as independent groups, and the cluster process was reiterated to reduce cluster size by 1 until cluster means were ≥ 1.96

SD separable (**C**). Results were de-convoluted and presented as (**D**) graph (*left*; mean [95% CI]) and topography map (*right*) formats with legend (*middle*). Clusters were separated into negative or positive ranks based on magnitude of normal difference (µm) and represented via a gradient color scale: $C_{-1,\ -2,\ -3,\ \ldots}$ = more thinned (*darker blue*; $C_{+1,\ +2,\ +3,\ \ldots}$ = more thickened (darker *green*). C_0 indicates within 1.96 SD of zero normal difference (*cream*). In the topography map, this example shows greater thinned (*darker blue*) retina toward the peripheral macula and greater thickened (*dark green*) retina centrally. The *black cross* denotes the foveal center; the scale at the *bottom right* and all images are in right-eye format.

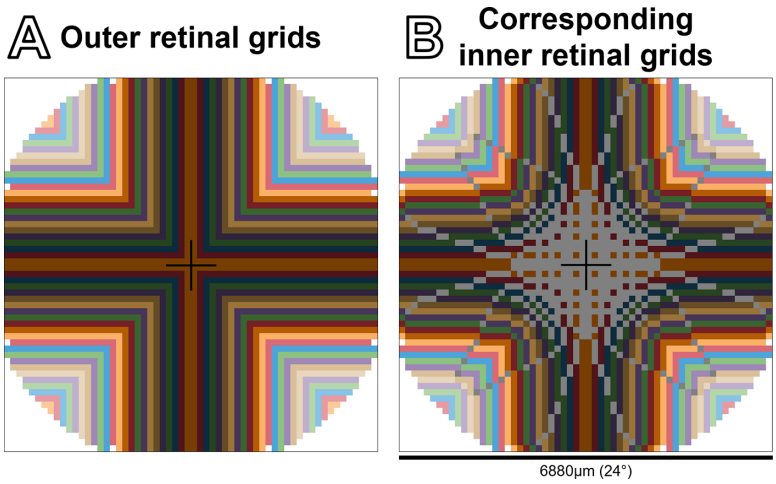

Figure 2. Comparisons between the outer and inner retinal grids according to the displacement function of Drasdo et al.[15] Corresponding grids between the (**A**) outer retina (RPE–BM, IS/OS, or ONL_{+HFL}) and (**B**) inner retina (IPL or GCL) are indicated by color in the columns and rows. Inner retinal grids that did not have a corresponding outer retinal grid are *gray*. Retinal grids that were unadjusted for displacement are *white*. The *middle black cross* denotes the foveal center.

ordered grids[46] using the log-likelihood method[47] to generate a suitable cluster number for each individual retinal layer while considering the lowest Bayesian information criterion, intracluster similarity, and intercluster separability.[48] Subsequently within each retinal layer, cluster means were compared and, if the separability criterion of ≥1.96 SD was not met, the cluster number was reduced and the cluster process reiterated until the criterion was satisfied (Fig. 1C). Note that by definition, the criterion of ≥1.96 SD ensured statistical difference between cluster means within each layer and is equivalent to $d' = 1.96$ from signal detection theory[49] and 95th-percentile normal distribution.

Final clusters for each retinal layer were deconvoluted to generate mean and confidence intervals and were displayed as graphs and spatial topography maps (Fig. 1D). Clusters were labeled as negative or positive and ranked based on the magnitude of normal difference (µm), represented via a gradient color scale for ease of interpretation: $C_{-1,\ -2,\ -3,\ \ldots}$ = more thinned (darker blue); $C_{+1,\ +2,\ +3,\ \ldots}$ = more thickened (darker green). C_0 indicates within 1.96 SD of zero normal difference (cream). Normal differences (µm) were also expressed in SD units (i.e., *Z*-scores calculated using mean and distribution of the sampled corrected normal population). Note that normal differences (SD units) are not statistically equivalent to the SD of normal differences (µm), as the latter is calculated using means and distributions of both sampled AMD and corrected normal populations.[50] Cluster normal differences (µm) were compared against eccentricity (mm) to determine potential effects of eccentricity in each layer. The RNFL was excluded from eccentricity comparisons due to its nasal to temporal (rather than concentric) distribution.[51]

Interlayer Correlation Analysis

To determine whether normal differences between retinal layers were related, gridwise correlations for AMD_{total} eyes were performed for all combinations of the GCL, IPL, INL, OPL, ONL_{+HFL}, IS/OS, and RPE–BM. The RNFL was excluded due to its relatively complex topographic localization with other retinal layers.[52] Correlations between the inner retina (namely, the GCL or IPL) versus the outer retina (namely, the ONL_{+HFL}, IS/OS, or RPE–BM) were adjusted according to the displacement function of ganglion cells from their cone inner segments averaged from principal meridians as described by Drasdo et al.[15] Specifically, average eccentricity of each outer retinal grid was plotted using an Akima spline, and subsequent displacement (along the same angular plane from the fovea) of each corresponding inner retinal grid was interpolated. Each outer retinal grid (Fig. 2A) was then correlated against the corresponding displaced inner retinal grids (Fig. 2B). In cases where some outer retinal grids corresponded to more than one inner retinal grid, these inner retinal grids were averaged. Thus, some outer retinal grids remained without a corresponding inner retinal grid (396/3600) (Fig. 2B, gray) and were excluded from interlayer comparisons that adjusted for displacement. Other retinal grids (544/3600) (Figs. 2A, 2B, white) were not adjusted for displacement, as their eccentricities lay beyond the displacement function.[15] Adjustments for the OPL and INL were not performed due to lack of available formulae in the

Investigative Ophthalmology & Visual Science

literature. Results were converted to absolute correlations ($|r|$) to focus on strength of the relationships.[53]

Dose–Response Analyses

Dose–response relationships were explored to address possible cause and effect between (1) AMD and retinal thickness normal differences,[54,55] and (2) AMD interlayer normal differences. First, cluster analysis was repeated for and then compared between AMD_{early} and AMD_{int} eyes. Cluster normal differences were calculated using AMD_{total} clusters, as these were assigned in consideration of statistically similar normal differences between disease severities. Second, interlayer correlation analysis was also repeated for and then compared between AMD_{early} and AMD_{int} eyes. Resultant values were denoted as severity differences.

Statistical Analysis

Statistical analyses were performed using Prism 9.2 (GraphPad, San Diego, CA, USA), SPSS Statistics 25 (IBM Corp., Armonk, NY, USA), and Excel 2108 (Microsoft, Redmond, WA, USA). Significance was considered as $P < 0.05$. Sex was dummy coded for regression modeling (i.e., males = 0 and females = 1). Normality was tested using the D'Agostino–Pearson test. Comparisons were performed using each participant's data as a single unit of observation rather than each grid where possible, the former representing unpaired or unrelated observations. Single comparisons between continuous variables (including cluster normal differences) were then performed using unpaired Student's *t*-tests or Mann–Whitney *U* tests depending on normality. Comparisons between related continuous variables (i.e., within-layer cluster comparisons) were performed using a mixed-effects, repeated-measures model with nonassumption of sphericity (equal variability of differences; Geisser–Greenhouse correction) and Holm–Sidak's multiple comparisons test. Comparisons between categorical variables were performed using Fisher's exact test. Comparisons between paired proportions (i.e., cluster area asymmetry comparisons) were performed using McNemar's test. Multiple single comparisons of unpaired observations were performed using unpaired Student's *t*-tests or Mann–Whitney *U* tests without adjustment. No statistical adjustment was performed, as each comparison was considered individually important[56]; instead, these results were considered contextually among all other results. Normal differences in SD units were interpreted according to Cohen's effect sizes: ≥0.2 = small, ≥0.5 = medium, and ≥0.8 = large.[57] Correlational analyses were performed using Pearson's correlation coefficient.[57] Correlation strength were interpreted according to Schober et al.,[58] such that $|r| < 0.1$ = negligible, $|r| < 0.4$ = weak, $|r| < 0.7$ = moderate, $|r| < 0.9$ = strong, and $|r| \geq 0.9$ = very strong. Correlation coefficients were transformed using Fisher's *Z*-transformation for comparisons, then back-transformed.[59]

Results

Participant Demographics

One eye from each of a total of 192 individual participants was used in this study: 96 AMD_{total} eyes (48 AMD_{early}, 48 AMD_{int}) and 96 normal eyes. Expectedly, there were no significant differences regarding age, sex, or spherical equivalent refraction among any groups following propensity-score matching (Table).

Topographical Differences in the Inner Retina Via Cluster Analysis

Gridwise thicknesses of each layer were compared between AMD_{total} and corrected normal eyes, and resultant normal differences were clustered. The cluster means of each individual retinal layer were established to be separable by ≥1.96 SD and further statistically confirmed using a mixed-effects, repeated-measures model and Holm–Sidak's multiple comparisons test ($P < 0.0001$ for all). For the RNFL, grids were assigned into three clusters that were all thinned relative to normal ($C_{-3,\ -2,\ -1}$) (Fig. 3A). There was extensively thinned RNFL inferiorly and partly superiorly in AMD_{total} eyes (C_{-3} mean, −8.13 µm; 95% CI, −11.12 to −5.13 and C_{-2} mean, −3.47 µm; 95% CI, −4.91 to −2.03) ($P < 0.0001$ for both) (Figs. 3A, 3B) that occupied half (49.7%) of the macula scan area. The asymmetry was confirmed with spatial division of $C_{-3,\ -2}$ into halves (Supplementary Fig. S1A), whereby $C_{-3,\ -2}$ had more extensive coverage in the inferior than superior half (34.7% vs. 15%, respectively; $P < 0.0001$). The remaining scan area (C_{-1}, 50.4%) was slightly thinned (−0.77 µm; 95% CI, −1.46 to −0.07; $P < 0.01$). Large effect sizes (*Z*-scores calculated using the mean and distribution of the sampled corrected normal population) were observed in C_{-3} and C_{-2} (−1.62 SD and −1.6 SD, respectively), whereas C_{-1} had medium effect size (−0.53 SD). Exact cluster sizes and normal differences are provided in Supplementary Table S1.

For the GCL, grids were assigned into three clusters, again mostly exhibiting thinned normal differences ($C_{-2,\ -1}$) (Fig. 3C). The thinned GCL clusters were located paracentrally and at the peripheral macula more so superiorly and temporally (C_{-2} mean, −2.49 µm; 95% CI, −3.5 to 1.47; $P < 0.0001$ and C_{-1} mean, −0.67 µm; 95% CI, −1.2 to −0.14; $P < 0.01$) (Figs. 3C, 3D), accommodating 78.1% of the macular scan area. Large effect sizes were observed in these thinned

Table. AMD and Normal Participant Demographics, Including Separate AMD_{early} and AMD_{int} Groups

	AMD_{total}	Normal	*P*	AMD_{early}	AMD_{int}	*P*
Eyes, *n*	96	96	—	48	48	—
Age (y), mean ± SD	66.4 ± 7.33	64.5 ± 7.73	0.09*	66.95 ± 7.37	65.81 ± 7.33	0.45*
Sex (females:males), *n*	63:33	51:45	0.11†	33:15	30:18	0.67†
Spherical equivalent refraction (D), mean ± SD	0.26 ± 1.37	0.15 ± 1.73	0.65*	0.1 ± 1.57	0.42 ± 1.12	0.26*

* Student's *t*-test.
† Fisher's exact test.

Investigative Ophthalmology & Visual Science

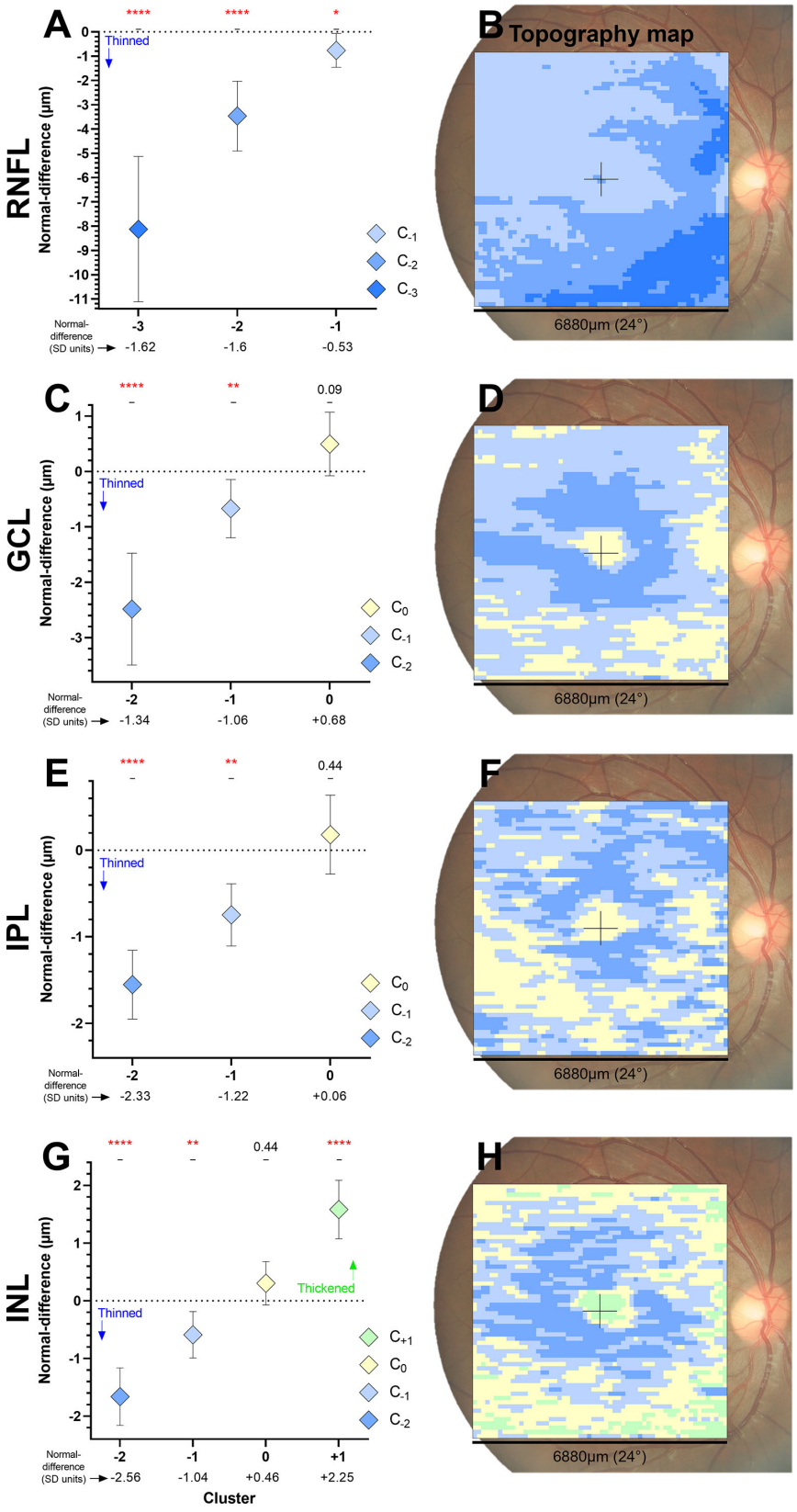

Figure 3. Cluster analysis for AMD_{total} eyes in the inner retina. Normal differences (µm) for each cluster are presented as graphs (mean [95% CI]) for the (**A**) RNFL, (**C**) GCL, (**E**) IPL, and (**G**) INL, with significance above each data point from unpaired Student's *t*-tests or Mann–Whitney *U* tests: **P* < 0.05, ***P* < 0.01, ****P* < 0.001, *****P* < 0.0001. Normal differences in SD units are included below the *x*-axis. Normal differences for each cluster are then presented as topography maps for the (**B**) RNFL, (**D**) GCL, (**F**) IPL, and (**H**) INL. Presentation is as described for Figure 1D.

clusters ($C_{-2,}$ −1.34 SD; C_{-1}, −1.06 SD). Asymmetry was confirmed with division of $C_{-2,\ -1}$ into quadrants (Supplementary Fig. S1B), with more coverage in the superior than inferior (23% vs. 16.2%, respectively; $P < 0.0001$) and temporal than nasal quadrants (23.1% vs. 17.9%, respectively; $P < 0.0001$). The linear regression slope of the GCL cluster normal difference (µm) versus eccentricity (µm) was significant ($C_{-2,\ -1,\ 0}$, $\beta = 0.71$; 95% CI, 0.67–0.75; $P < 0.0001$), implying thinned GCL (which began paracentrally) was lessened with increasing eccentricity. There was no GCL normal difference centrally or at parts of the peripheral macula, particularly inferiorly and nasally (C_0, 0.5; 95% CI, −0.08 to 1.07; $P = 0.09$).

Analysis of the IPL grids led to three assigned clusters ($C_{-2,\ -1,\ 0}$) (Fig. 3E). There was extensively thinned IPL covering 70% of the macular scan area (C_{-2}, −1.55 µm; 95% CI, −1.95 to −1.16; $P < 0.0001$ and C_{-1}, −0.75 µm; 95% CI, −1.11 to −0.39; $P < 0.01$) (Figs. 3E, 3F) with large effect sizes (C_{-2}, −2.33 SD; C_{-1}, −1.22 SD). Scattered parts of the IPL showed no normal difference, more so toward the peripheral macula and inferiorly (C_0, 0.18 µm; 95% CI, −0.28 to 0.64; $P = 0.44$; 30% macular scan area). Correspondingly, there was more coverage of $C_{-2,\ -1}$ in the superior than inferior quadrant (22.7% vs. 15.8%, respectively; $P < 0.0001$). These results were supported by the linear regression slope of IPL cluster normal difference versus eccentricity, which was significant ($C_{-2,\ -1,\ 0}$, $\beta = 0.08$; 95% CI, 0.04 to 0.12; $P < 0.001$), implying lesser thinned IPL with increasing eccentricity.

Analysis of the INL grids led to four assigned clusters ($C_{-2,\ -1,\ 0,\ +1}$) (Fig. 3G). The two thinned clusters ($C_{-2,}$ −1.66 µm; 95% CI, −2.16 to −1.16; $P < 0.0001$ and C_{-1}, −0.59 µm; 95% CI, −0.99 to −0.19; $P < 0.05$) (Figs. 3G, 3H) were situated paracentrally and comprised a majority of the macular scan area (55.2%) with large effect sizes ($C_{-2,}$ −2.56 SD; C_{-1}, −1.04 SD). The remaining clusters showed either no normal difference (C_0, 0.3; 95% CI, −0.07 to 0.68; $P = 0.44$) or thickened INL (C_{+1}, 1.58 µm; 95% CI, 1.07–2.09; $P < 0.0001$; 8.9% macular scan area) at the central and peripheral macula. The thickened INL (C_{+1}) had a large effect size (2.25 SD). The linear regression slope of INL clusters was significant ($C_{-2,\ -1,\ 0,\ +1}$, $\beta = 0.55$; 95% CI, 0.51–0.58; $P < 0.0001$) and implied lesser thinned and greater thickened INL with increasing eccentricity.

Topographical Differences in the Outer Retina Via Cluster Analysis

For the OPL and ONL_{+HFL}, analyses of each individual layer revealed an inverted topographical pattern of the other (Supplementary Fig. S2). This suggested that disorganization of the HFL could potentially be creating artifactual interrelated cluster results in the OPL and ONL_{+HFL}. Subsequently, the two layers were combined into the OPL/ONL_{+HFL}, and two clusters were assigned ($C_{-1,\ 0}$) (Fig. 4A). There was thinned OPL/ONL_{+HFL} scattered paracentrally and peripherally, mostly superiorly and inferiorly (C_{-1}, −1.31 µm; 95% CI, −2.06 to −0.55; $P < 0.05$; 68.3% macular scan area) (Figs. 4A, 4B) with large effect size (C_{-1}, −1.87 SD). The remaining area (31.7% macular scan area) showed non-significant normal difference (C_0, 0.37 µm; 95% CI, −0.47 to 1.18; $P = 0.58$). The linear regression slope was significant ($C_{-1,\ 0}$, $\beta = -0.26$; 95% CI, −0.33 to −0.2; $P < 0.0001$). This implied greater thinned OPL/ONL_{+HFL} with increasing eccentricity.

For the IS/OS, grids were assigned to two clusters ($C_{-1,\ 0}$) (Fig. 4C). Only the central cluster was significant showing thinned IS/OS (C_{-1}, −1.25 µm; 95% CI, −2.1 to −0.41; $P < 0.001$; 3.6% macular scan area) (Figs. 4C, 4D) with large effect size (C_{-1}, −1.47 SD). The remaining non-central cluster showed non-significant normal differences (C_0, 0.19 µm; 95% CI, −0.38 to 0.75; $P = 0.52$). The linear regression slope was significant ($C_{-1,\ 0}$, $\beta = 1.99$; 95% CI, 1.96 to 2.01; $P < 0.0001$) and implied lesser thinned IS/OS with greater eccentricity.

Finally, RPE−BM grids were assigned to three clusters ($C_{-1,\ +1,\ +2}$) (Fig. 4E), with thickened RPE−BM centrally ($C_{+1,}$ 0.62 µm; 95% CI, 0.29–0.96; $P < 0.01$ and C_{+2}, 2.99 µm; 95% CI, 0.97–5.01; $P < 0.0001$; 41.3% scan area) (Figs. 4E, 4F) with large effect sizes (C_{+1}, 2.54 SD; C_{+2}, 9.93 SD), and thinned RPE−BM peripherally (C_{-1}, −0.28 µm; 95% CI, −0.54 to −0.04; $P < 0.01$; 58.8% scan area) with large effect size (C_{-1}, −1.05 SD). An eccentricity effect was supported by the linear regression slope, which was significant ($C_{-1,\ +1,\ +2}$, $\beta = -0.52$; 95% CI, −0.54 to −0.49; $P < 0.0001$) and implied greater thinned and lesser thickened RPE−BM with increasing eccentricity.

Interlayer Correlation Analysis

To then determine whether normal differences between different retinal layers were related, gridwise correlations for AMD_{total} eyes were performed for all combinations of the GCL, IPL, INL, OPL, ONL_{+HFL}, IS/OS, and RPE–BM. The OPL and ONL_{+HFL} were analyzed individually because interlayer correlation analysis compares gridwise thicknesses and should be unaffected by artifactual interrelated clustering, unlike cluster analysis. Correlations between the GCL or IPL versus the ONL_{+HFL}, IS/OS, or RPE–BM included adjustment for displacement of Henle's fibers.

Overall interlayer mean correlations were negligible-to-moderate strength (0.09 ± 0.09 to 0.46 ± 0.19). This was regardless of the number of statistically significant grids associated with correlations (458/3600 to 2987/3600 grids, $P < 0.05$). Correlations were strongest in the GCL versus IPL ($|r|$ mean ± SD, 0.46 ± 0.19; 3141/3600 grids significant), GCL versus INL ($|r|$ mean ± SD, 0.24 ± 0.14; 2009/3600 grids significant), INL versus OPL ($|r|$ mean ± SD, 0.22 ± 0.14; 1712/3600 grids significant), and OPL versus ONL_{+HFL} ($|r|$ mean ± SD, 0.22 ± 0.19; 1352/3600 grids significant) (Fig. 5).

Dose–Response Analyses

Finally, dose–response analyses were performed to determine if topographical differences and interlayer correlations were associated with AMD severity. First, cluster normal differences (µm) were recalculated for AMD_{early} and AMD_{int} eyes as separate groups (Supplementary Table S2). All clusters for AMD_{early} and AMD_{int} eyes showed consistent direction of significant normal differences; for example, a cluster that demonstrated significantly thinned retina for AMD_{early} was also thinned for AMD_{int}, albeit with different magnitudes. Normal differences of AMD_{early} were then subtracted from AMD_{int} eyes, and resultant values were denoted as severity differences (µm). Comparing AMD_{int} and AMD_{early} eyes, severity differences were positive in most clusters

Investigative Ophthalmology & Visual Science

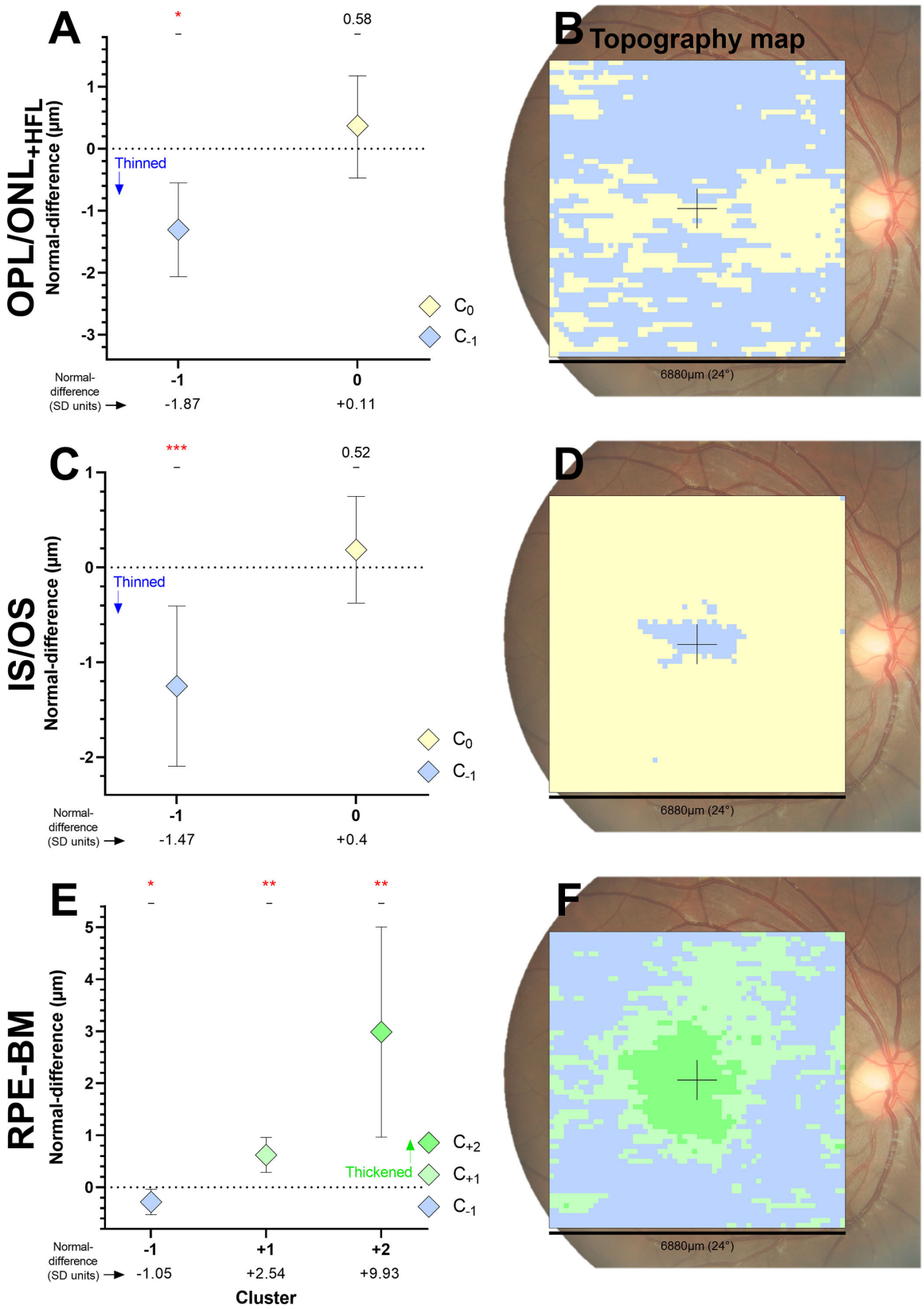

Figure 4. Cluster analysis for AMD_{total} eyes in the outer retina. Normal differences (µm) for each cluster are presented as graphs (mean [95% CI]) for the (**A**) OPL/ONL_{+HFL}, (**C**) IS/OS, and (**E**) RPE–BM and as topography maps for the (**B**) OPL/ONL_{+HFL}, (**D**) IS/OS, and (**F**) RPE–BM. Presentation is as described in Figure 1D.

Investigative Ophthalmology & Visual Science

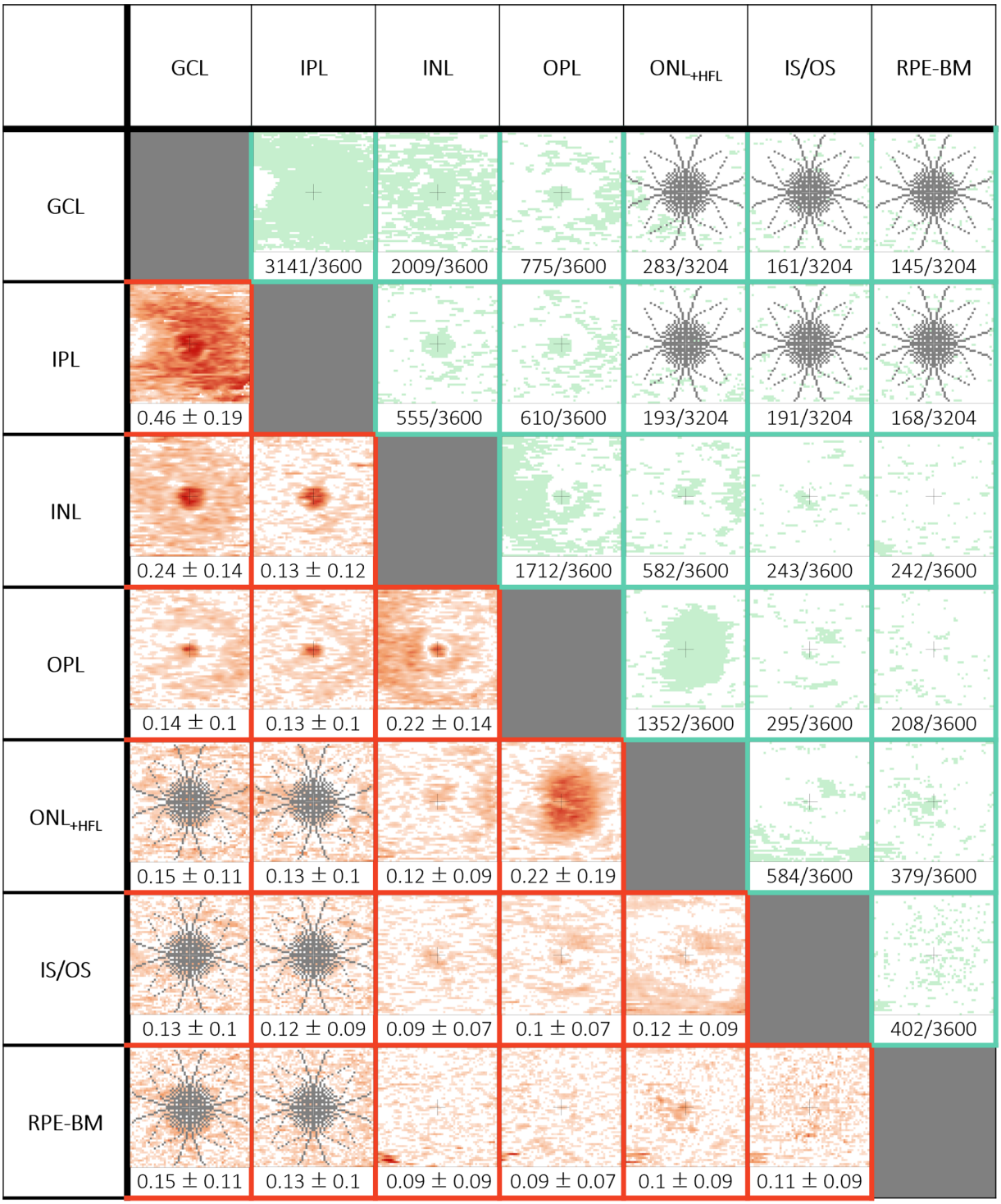

Figure 5. Interlayer correlation analysis for AMD_{total} eyes. The strength of correlation is presented in *red* (*left*) *cells*, where $|r|$ is expressed as mean ± SD and pictorially represented on a shaded gradient scale: $|r| = 0.1$ to $|r| = 0.5$ to $|r| > 0.9$ (*light orange* to *red*); $|r| < 0.1$ (*white*). The number of statistically significant grids is presented in *green* (*right*) *cells*, expressed as counts and pictorially represented as *light green* shading: $P < 0.05$. Note that there are 3600 total grids but 3204 grids after adjustment for the displacement of Henle's fibers for comparisons between the GCL or IPL versus the ONL_{+HFL}, IS/OS, or RPE–BM.15 Excluded grids are shown in *gray*.

of all layers (Supplementary Table S2), suggesting mostly thicker retina with greater AMD severity. This, however, only reached significance in the RPE–BM centrally (C_{+1}, 1.07 µm; 95% CI, 0.97–1.18; $P < 0.01$ and C_{+2}, 5.44 µm; 95% CI, 4.88–6.00; $P < 0.01$) (Figs. 6A, 6B). Second, interlayer correlations were recalculated for AMD_{early} and AMD_{int} eyes as separate groups (Supplementary Table S3). All correlations between AMD_{int} and AMD_{early} eyes were non-significant, highlighting that interlayer relationships were not affected by AMD severity.

Investigative Ophthalmology & Visual Science

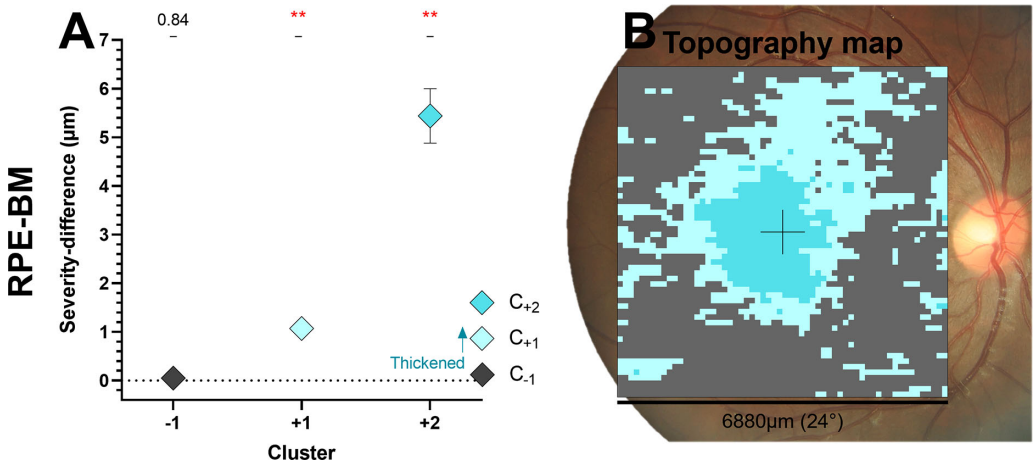

Figure 6. Dose–response cluster analysis comparing AMD_{int} and AMD_{early} eyes in the RPE–BM. Severity differences (µm) for each cluster are presented as (**A**) a graph (mean [95% CI]) and (**B**) a topography map. Presentation is as described in Figure 1C. Clusters are as described in Figures 4E and 4F. Cluster severity differences are represented via a gradient color scale: more thickened, *darker teal*; no significant difference, *gray*. No other retinal layers demonstrated significance severity differences.

Discussion

OCT high-density thickness analysis revealed anatomical differences between early/intermediate AMD and normal eyes with unique topography and large effect sizes across all retinal layers. Interestingly, differences between retinal layers were not strongly related or affected by disease severity, suggesting that it is unlikely that there is a localized cause and effect between outer retinal to inner retinal changes. These results imply that thickness differences across all retinal layers are established from early AMD, and that clinical OCT assessment of the outer retina alone does not sufficiently depict complete retinal integrity in early/intermediate AMD.

Anatomical Differences Present Across All Retinal Layers from Early AMD

AMD eyes displayed concurrent anatomical topographical differences from normal across all retinal layers, present in early and intermediate AMD. In the inner retina, previous studies comparing early and/or intermediate AMD to normal eyes across global or low-density areas have reported mostly thinned GCL and IPL,[3–10,60,61] in agreement with our current results, possibly signifying reduced density of ganglion cells and their synapses with INL neurons.[62] Expectedly, studies have also reported reduced peripapillary RNFL thicknesses in early/intermediate AMD,[10,60] although, puzzlingly, many studies suggest that the macular RNFL is unaltered,[3,5–7] possibly due to sparse distribution at the macula.[23,51,63–66] Recently, our moderate-density analysis highlighted potential changes in the macular RNFL of intermediate AMD eyes, although with an indistinguishable topographical pattern.[17] The greater (56×) lateral resolution and modified cluster application afforded by the current study confirms extensively thinned macular RNFL in both early and intermediate AMD eyes which now corresponds to the concomitantly thinned underlying GCL.

Previous studies have also reported thinned INL via global or low-density retinal assessments in early and/or intermediate AMD compared to normal eyes,[3–5] possibly signifying reduced densities of bipolar, horizontal, amacrine, and/or Müller cells.[67] Our spatially refined topographical analysis confirms that the thinned INL is mostly paracentral, but it also revealed that there was less thinned and greater thickened INL with increasing eccentricity which may be associated with changes in INL neurons and/or glia (Müller) cells with comparable topography.[24,67–69] Thickening in the INL may be further corroborated by other studies describing inner retinal remodeling in outer retinal degenerations, such as outgrowth of rod bipolar dendrites[70] and horizontal and amacrine cell neurites[71] and upregulation of Müller cells.[72–74] Thickened INL centrally, on the other hand, was peculiar considering that there should be an almost nonexistent cellular population within ~1 mm eccentricity,[67,69] and it may represent distortion of retinal layers from underlying drusenoid elevations rather than true cellular proliferation or hypertrophy.

In the outer retina, previous studies using global or low-density spatial assessments of early and/or intermediate AMD eyes compared to normal have reported thinned OPL, ONL, and/or IS/OS[3,5,75–77] and thickened RPE–BM.[3,5,78–80] Our preceding moderate-density analysis indicated thinned OPL and ONL_{+HFL}, no significant IS/OS differences, and thickened RPE–BM centrally.[17] Accordingly, our current high-density analyses upheld these findings and revealed some additional details. The OPL/ONL_{+HFL} and RPE–BM were more greatly thinned with increasing eccentricity, which may relate to rod susceptibility in AMD[24,25,81] reflected in structural[2,82–87] and functional[88–93] measures. The centrally thinned IS/OS could ambiguously be true outer segment loss, although this would not explain why noncentral areas are unaffected, or a mechanical disorientation of photoreceptor segments from underlying drusenoid elevations, as has been described with adaptive-optics OCT.[84]

Unexpected Cause-and-Effect Relationships

A series of studies including this one have revealed neuronal, synaptic, and even vascular differences across the inner and outer retina of AMD compared to normal eyes.[16,17,94] However, the relational implications of these findings are unclear. Using dose–response analysis, this study sought to

clarify whether there may be cause and effect between AMD and thickness normal differences across all retinal neuronal and synaptic layers. We observed that, from early to intermediate AMD, the central RPE–BM was thicker, expectedly reflecting increased drusen load. Additionally, the majority of clusters within all retinal layers were less thinned and more thickened, which interestingly may reinforce potential inner retinal remodeling in AMD as described above,[68,72–74] such as cellular hyperactivity and membrane hyperpermeability,[95] although none (except the RPE–BM) reached statistical significance. Nevertheless, the consistent direction of differences from normal early and intermediate AMD eyes reaffirms that topographical thickness differences are mostly established from early AMD and strengthen the likelihood that AMD is a causative factor of these differences rather than some unmeasured variable or random chance.

We also used dose–response analysis to assess interlayer normal differences which subsequently were not strongly related in early/intermediate AMD or affected by AMD severity.[17] This suggested that there is unlikely a localized cause-and-effect relationship between progressive outer retinal changes (such as thickened RPE–BM from accumulating drusen) and post-photoreceptor alterations (such as extensively thinned RNFL, GCL, IPL, and paracentral INL), as proposed in the anterograde transsynaptic[11] and ischemia postreceptoral degeneration[12] pathophysiological models of AMD. Alternatively, interlayer relationships in AMD may still exist locally via degenerative bioactive molecules[96,97] or some other mechanisms undetectable via OCT thickness analyses or, more broadly, via systemic inflammatory pathways.[98–101] Nonetheless, the lack of interlayer relationships in this study intimates that the extensive anatomical differences across all retinal layers in early/intermediate AMD cannot be assessed via OCT analysis of the outer retina alone. Greater focus on the inner retina may thus be warranted in the future clinically, as well as in the development of therapies for AMD such as optogenetics and prosthetic devices that rely upon sustained post-photoreceptoral health for intervention success.[95]

Limitations

The primary limitation of this study relates to inferences drawn from OCT thickness data that do not capture specifically which cellular and synaptic processes[67,102] nor physiological mechanisms may be altered in disease. Further development of our work with more comprehensive co-variable correction such as axial length, use of longitudinal data, and comparison to other measures of retinal integrity such as a high-magnification or adaptive-optics OCT could illuminate the relationship between inner and outer retinal changes in the early stages of AMD.

Additionally, although we demonstrated statistically significant anatomical topographical differences across all retinal layers, it is unclear whether these differences are clinically important. There are no established guidelines that define clinically important thickness differences for each individual retinal layer, particularly in the context of manual segmentation. To enable transparency of effect sizes and additionally account for varying thicknesses across the macula in each retinal layer, we reported thicknesses in both micrometers and SD units. Our dose–response analysis also helped to answer whether thickness differences within and between retinal layers in early/intermediate AMD are isolated phenomena or demonstrate any clinically detectable cause and effect. Future works will need to explore the clinical importance of thickness differences across all retinal layers.

Conclusions

Anatomical differences between early/intermediate AMD and normal eyes display unique topography with large effect sizes and are mostly established from the early stage. Interlayer differences, though, are not strongly related regardless of AMD severity. These results elucidate where changes may occur and emphasize that complete retinal integrity cannot be assessed via OCT of the outer retina alone in early/intermediate AMD.

Acknowledgments

The authors thank Janelle Tong (Centre for Eye Health, Sydney, Australia) for methodological advice and Vincent Khou (Centre for Eye Health, Sydney, Australia) for retinal layer segmentation.

Supported, in part, by grants from the National Health and Medical Research Council of Australia (NHMRC; 1186915 to MK and DAC and 1174385 to LNS) and by the Rebecca Cooper Foundation. MT is supported by an Australian Research Training Program scholarship. Guide Dogs NSW/ACT provides support for the Centre for Eye Health (the clinic of recruitment) and salary support for MK.

Disclosure: **M. Trinh**, None; **M. Kalloniatis**, None; **D. Alonso-Caneiro**, None; **L. Nivison-Smith**, None

References

1. Ambati J, Ambati BK, Yoo SH, Ianchulev S, Adamis AP. Age-related macular degeneration: etiology, pathogenesis, and therapeutic strategies. *Surv Ophthalmol*. 2003;48:257–293.
2. Curcio CA, Medeiros NE, Millican CL. Photoreceptor loss in age-related macular degeneration. *Invest Ophthalmol Vis Sci*. 1996;37:1236–1249.
3. Brandl C, et al. Retinal layer thicknesses in early age-related macular degeneration: results from the German AugUR study. *Invest Ophthalmol Vis Sci*. 2019;60:1581–1594.
4. Savastano MC, et al. Differential vulnerability of retinal layers to early age-related macular degeneration: evidence by SD-OCT segmentation analysis. *Invest Ophthalmol Vis Sci*. 2014;55:560–566.
5. Lamin A, Oakley JD, Dubis AM, Russakoff DB, Sivaprasad S. Changes in volume of various retinal layers over time in early and intermediate age-related macular degeneration. *Eye (Lond)*. 2019;33:428–434.
6. Muftuoglu IK, et al. Quantitative analysis of the inner retinal layer thicknesses in age-related macular degeneration using corrected optical coherence tomography segmentation. *Retina*. 2018;38:1478–1484.
7. Borrelli E, et al. Postreceptor neuronal loss in intermediate age-related macular degeneration. *Am J Ophthalmol*. 2017;181:1–11.
8. Yenice E, Şengün A, Soyugelen Demirok G, Turaçlı E. Ganglion cell complex thickness in nonexudative age-related macular degeneration. *Eye (Lond)*. 2015;29:1076–1080.
9. Zucchiatti I, et al. Macular ganglion cell complex and retinal nerve fiber layer comparison in different stages of age-related macular degeneration. *Am J Ophthalmol*. 2015;160:602–607.e1.

10. Lee EK, Yu HG. Ganglion cell-inner plexiform layer and peripapillary retinal nerve fiber layer thicknesses in age-related macular degeneration. *Invest Ophthalmol Vis Sci*. 2015;56:3976–3983.
11. Panneman EL, Coric D, Tran LMD, de Vries-Knoppert WAEJ, Petzold A. Progression of anterograde trans-synaptic degeneration in the human retina is modulated by axonal convergence and divergence. *Neuroophthalmology*. 2019;43:382–390.
12. Feigl B, Brown B, Lovie-Kitchin J, Swann P. Functional loss in early age-related maculopathy: the ischaemia postreceptoral hypothesis. *Eye (Lond)*. 2007;21:689–696.
13. Wong DWS. The modifiable areal unit problem (MAUP). In: Janelle DG, Warf B, Hansen K , eds. *WorldMinds: Geographical Perspectives on 100 Problems: Commemorating the 100th Anniversary of the Association of American Geographers 1904–2004*. Heidelberg: Springer; 2004:571–575.
14. Jelinski DE, Wu J. The modifiable areal unit problem and implications for landscape ecology. *Landsc Ecol*. 1996;11:129–140.
15. Drasdo N, Millican CL, Katholi CR, Curcio CA. The length of Henle fibers in the human retina and a model of ganglion receptive field density in the visual field. *Vision Res*. 2007;47:2901–2911.
16. Trinh M, et al. Macula ganglion cell thickness changes display location-specific variation patterns in intermediate age-related macular degeneration. *Invest Ophthalmol Vis Sci*. 2020;61:2.
17. Trinh M, Khou V, Kalloniatis M, Nivison-Smith L. Location-specific thickness patterns in intermediate age-related macular degeneration reveals anatomical differences in multiple retinal layers. *Invest Ophthalmol Vis Sci*. 2021;62:13.
18. Trinh M, Kalloniatis M, Nivison-Smith L. Location-specific patterns of inner retinal thinning in intermediate age-related macular degeneration. *Invest Ophthalmol Vis Sci*. 2021;62:305.
19. Trinh M, Khou V, Zangerl B, Kalloniatis M, Nivison-Smith L. Modelling normal age-related changes in individual retinal layers using location-specific OCT analysis. *Sci Rep*. 2021;11:558.
20. Tong J, et al. Development of a spatial model of age-related change in the macular ganglion cell layer to predict function from structural changes. *Am J Ophthalmol*. 2019;208:166–177.
21. Yoshioka N, et al. Pattern recognition analysis of age-related retinal ganglion cell signatures in the human eye. *Invest Ophthalmol Vis Sci*. 2017;58:3086–3099.
22. Curcio CA, Allen KA. Topography of ganglion cells in human retina. *J Comp Neurol*. 1990;300:5–25.
23. Blumenthal E, et al. Retinal nerve fibre layer imaging compared with histological measurements in a human eye. *Eye (Lond)*. 2007;23:171–175.
24. Lee SCS, Martin PR, Grünert U. Topography of neurons in the rod pathway of human retina. *Invest Ophthalmol Vis Sci*. 2019;60:2848–2859.
25. Ahnelt PK. The photoreceptor mosaic. *Eye (Lond)*. 1998;12:531–540.
26. Ach T, et al. Quantitative autofluorescence and cell density maps of the human retinal pigment epithelium. *Invest Ophthalmol Vis Sci*. 2014;55:4832–4841.
27. Khou V, et al. Development of a high-density spatially localized model of the human retina. *Invest Ophthalmol Vis Sci*. 2020;61:497–497.
28. Wang H, Kalloniatis M. Clinical outcomes of the Centre for Eye Health: an intra-professional optometry-led collaborative eye care clinic in Australia. *Clin Exp Optom*. 2021;104:795–804.
29. Ferris FL, et al. Clinical classification of age-related macular degeneration. *Ophthalmology*. 2013;120:844–851.
30. Sleiman K, et al. Optical coherence tomography predictors of risk for progression to non-neovascular atrophic age-related macular degeneration. *Ophthalmology*. 2017;124:1764–1777.
31. Hallak JA, et al. Imaging, genetic, and demographic factors associated with conversion to neovascular age-related macular degeneration: secondary analysis of a randomized clinical trial. *JAMA Ophthalmol*. 2019;137:738–744.
32. Waldstein SM, et al. Characterization of drusen and hyperreflective foci as biomarkers for disease progression in age-related macular degeneration using artificial intelligence in optical coherence tomography. *JAMA Ophthalmol*. 2020;138:740–747.
33. Guymer RH, et al. Proof of concept, randomized, placebo-controlled study of the effect of simvastatin on the course of age-related macular degeneration. *PLoS One*. 2013;8:e83759.
34. Rosenbaum PR, Rubin DB. Constructing a control group using multivariate matched sampling methods that incorporate the propensity score. *Am Stat*. 1985;39:33–38.
35. Stuart EA. Matching methods for causal inference: a review and a look forward. *Stat Sci*. 2010;25:1–21.
36. Lunt M. Selecting an appropriate caliper can be essential for achieving good balance with propensity score matching. *Am J Epidemiol*. 2014;179:226–235.
37. Heidelberg Engineering GmbH. *SPECTRALIS®. Glaucoma Module Premium Edition. User Manual Software Version 6.7*. Heidelberg, Germany: Heidelberg Engineering GmbH; 2016.
38. Camacho P, Dutra-Medeiros M, Salgueiro L, Sadio S, Rosa PC. Manual segmentation of 12 layers of the retina and choroid through SD-OCT in intermediate AMD: repeatability and reproducibility. *J Ophthalmic Vis Res*. 2021;16:384–392.
39. Tian J, et al. Performance evaluation of automated segmentation software on optical coherence tomography volume data. *J Biophotonics*. 2016;9:478–489.
40. Maloca PM, et al. Validation of automated artificial intelligence segmentation of optical coherence tomography images. *PLoS One*. 2019;14:e0220063.
41. de Azevedo AGB, et al. Impact of manual correction over automated segmentation of spectral domain optical coherence tomography. *Int J Retina Vitreous*. 2020;6:4.
42. Gaurisankar ZS, et al. Correlations between ocular biometrics and refractive error: a systematic review and meta-analysis. *Acta Ophthalmol*. 2019;97:735–743.
43. Frades I, Matthiesen R. Overview on techniques in cluster analysis. *Methods Mol Biol*. 2010;593:81–107.
44. Palazon-Cabanes A, et al. Normative database for all retinal layer thicknesses using SD-OCT posterior pole algorithm and the effects of age, gender and axial length. *J Clin Med*. 2020;9:3317.
45. Gelbard R, Goldman O, Spiegler I. Investigating diversity of clustering methods: an empirical comparison. *Data Knowl Eng*. 2007;63:155–166.
46. Vichi M. *Data Science: Innovative Developments in Data Analysis and Clustering*. Cham, Switzerland: Springer Nature; 2017.
47. Raykov YP, Boukouvalas A, Baig F, Little MA. What to do when K-means clustering fails: a simple yet principled alternative algorithm. *PLoS One*. 2016;11:e0162259.
48. Bacher J, Wenzig K, Vogler M. *SPSS TwoStep Cluster – a first evaluation*. Nürnberg: Sozialwissenschaftliches Institut,

Investigative Ophthalmology & Visual Science

Lehrstuhl für Soziologie, Universität Erlangen-Nürnberg; 2004.
49. Macmillan N, Creelman D. *Detection Theory: A User's Guide*. 2nd ed. New York: Routledge; 2004.
50. DeVore GR. Computing the Z score and centiles for cross-sectional analysis: a practical approach. *J Ultrasound Med*. 2017;36:459–473.
51. Varma R, Skaf M, Barron E. Retinal nerve fiber layer thickness in normal human eyes. *Ophthalmology*. 1996;103:2114–2119.
52. Kim KE, et al. Topographic localization of macular retinal ganglion cell loss associated with localized peripapillary retinal nerve fiber layer defect. *Invest Ophthalmol Vis Sci*. 2014;55:3501–3508.
53. Aggarwal R, Ranganathan P. Common pitfalls in statistical analysis: the use of correlation techniques. *Perspect Clin Res*. 2016;7:187–190.
54. Guyatt GH, et al. GRADE guidelines: 9. Rating up the quality of evidence. *J Clin Epidemiol*. 2011;64:1311–1316.
55. Rutter M. Beyond longitudinal data: causes, consequences, changes, and continuity. *J Consult Clin Psychol*. 1994;62:928–940.
56. Armstrong RA. When to use the Bonferroni correction. *Ophthalmic Physiol Opt*. 2014;34:502–508.
57. Cohen J. *Statistical Power Analysis for the Behavioral Sciences*. Mahwah, NJ: Lawrence Erlbaum Associates; 1988.
58. Schober P, Boer C, Schwarte LA. Correlation coefficients: appropriate use and interpretation. *Anesth Analg*. 2018;126:1763–1768.
59. Cox NJ. Speaking Stata: correlation with confidence, or Fisher's z revisited. *Stata J*. 2008;8:413–439.
60. Shin I-H, Lee W-H, Lee J-J, Jo Y-J, Kim J-Y. Thickness of the macula, retinal nerve fibre layer, and ganglion cell-inner plexiform layer in age-related macular degeneration: the repeatability study of spectral domain optical coherence tomography. *Retina*. 2018;38:253–262.
61. Camacho P, Dutra-Medeiros M, Páris L. Ganglion cell complex in early and intermediate age-related macular degeneration: evidence by SD-OCT manual segmentation. *Ophthalmologica*. 2017;238:31–43.
62. Medeiros NE, Curcio CA. Preservation of ganglion cell layer neurons in age-related macular degeneration. *Invest Ophthalmol Vis Sci*. 2001;42:795–803.
63. Cohen MJ, et al. Morphometric analysis of human peripapillary retinal nerve fiber layer thickness. *Invest Ophthalmol Vis Sci*. 2008;49:941–944.
64. Frenkel S, Morgan JE, Blumenthal EZ. Histological measurement of retinal nerve fibre layer thickness. *Eye (Lond)*. 2005;19:491–498.
65. Blumenthal EZ. Quantifying retinal nerve fiber layer thickness histologically: a novel approach to sectioning of the retina. *Invest Ophthalmol Vis Sci*. 2004;45:1404–1409.
66. Dichtl A, Jonas JB, Naumann GO. Retinal nerve fiber layer thickness in human eyes. *Graefes Arch Clin Exp Ophthalmol*. 1999;237:474–479.
67. Masri RA, et al. Composition of the inner nuclear layer in human retina. *Invest Ophthalmol Vis Sci*. 2021;62:22.
68. Chua J, et al. Early remodeling of Müller cells in the rd/rd mouse model of retinal dystrophy. *J Comp Neurol*. 2013;521:2439–2453.
69. Martin P, Grünert U. Spatial density and immunoreactivity of bipolar cells in the macaque monkey. *J Comp Neurol*. 1992;323:269–287.
70. Sullivan RKP, WoldeMussie E, Pow DV. Dendritic and synaptic plasticity of neurons in the human age-related macular degeneration retina. *Invest Ophthalmol Vis Sci*. 2007;48:2782–2791.
71. Fariss RN, Li Z-Y, Milam AH. Abnormalities in rod photoreceptors, amacrine cells, and horizontal cells in human retinas with retinitis pigmentosa. *Am J Ophthalmol*. 2000;129:215–223.
72. Madigan MC, Penfold PL, Provis JM, Balind TK, Billson FA. Intermediate filament expression in human retinal macroglia. Histopathologic changes associated with age-related macular degeneration. *Retina*. 1994;14:65–74.
73. Wu KHC, Madigan MC, Billson FA, Penfold PL. Differential expression of GFAP in early v late AMD: a quantitative analysis. *Br J Ophthalmol*. 2003;87:1159–1166.
74. Johnson PT, et al. Drusen-associated degeneration in the retina. *Invest Ophthalmol Vis Sci*. 2003;44:4481–4488.
75. Schuman SG, et al. Photoreceptor layer thinning over drusen in eyes with age-related macular degeneration imaged in vivo with spectral-domain optical coherence tomography. *Ophthalmology*. 2009;116:488–496.e2.
76. Rogala J, et al. In vivo quantification of retinal changes associated with drusen in age-related macular degeneration. *Invest Ophthalmol Vis Sci*. 2015;56:1689–1700.
77. Sadigh S, et al. Abnormal thickening as well as thinning of the photoreceptor layer in intermediate age-related macular degeneration. *Invest Ophthalmol Vis Sci*. 2013;54:1603–1612.
78. Nivison-Smith L, Wang H, Assaad N, Kalloniatis M. Retinal thickness changes throughout the natural history of drusen in age-related macular degeneration. *Optom Vis Sci*. 2018;95:648–655.
79. Ferrara D, et al. Optical coherence tomography features preceding the onset of advanced age-related macular degeneration. *Invest Ophthalmol Vis Sci*. 2017;58:3519–3529.
80. Farsiu S, et al. Quantitative classification of eyes with and without intermediate age-related macular degeneration using optical coherence tomography. *Ophthalmology*. 2014;121:162–172.
81. Curcio CA, Sloan KR, Kalina RE, Hendrickson AE. Human photoreceptor topography. *J Comp Neurol*. 1990;292:497–523.
82. Godara P, Siebe C, Rha J, Michaelides M, Carroll J. Assessing the photoreceptor mosaic over drusen using adaptive optics and SD-OCT. *Ophthalmic Surg Lasers Imaging*. 2010;41:S104–S108.
83. Mrejen S, Sato T, Curcio CA, Spaide RF. Assessing the cone photoreceptor mosaic in eyes with pseudodrusen and soft drusen in vivo using adaptive optics imaging. *Ophthalmology*. 2014;121:545–551.
84. Reumueller A, et al. Three-dimensional adaptive optics-assisted visualization of photoreceptors in healthy and pathologically aged eyes. *Invest Ophthalmol Vis Sci*. 2019;60:1144–1155.
85. Querques G, et al. Appearance of medium–large drusen and reticular pseudodrusen on adaptive optics in age-related macular degeneration. *Br J Ophthalmol*. 2014;98:1522–1527.
86. Zayit-Soudry S, Duncan JL, Syed R, Menghini M, Roorda AJ. Cone structure imaged with adaptive optics scanning laser ophthalmoscopy in eyes with nonneovascular age-related macular degeneration. *Invest Ophthalmol Vis Sci*. 2013;54:7498–7509.
87. Boretsky A, et al. In vivo imaging of photoreceptor disruption associated with age-related macular degeneration: a pilot study. *Lasers Surg Med*. 2012;44:603–610.
88. Flamendorf J, et al. Impairments in dark adaptation are associated with age-related macular degeneration severity and reticular pseudodrusen. *Ophthalmology*. 2015;122:2053–2062.

Investigative Ophthalmology & Visual Science

89. Owsley C, McGwin G, Jackson GR, Kallies K, Clark M. Cone- and rod-mediated dark adaptation impairment in age-related maculopathy. *Ophthalmology*. 2007;114:1728–1735.
90. Owsley C, et al. Psychophysical evidence for rod vulnerability in age-related macular degeneration. *Invest Ophthalmol Vis Sci*. 2000;41:267–273.
91. Owsley C, et al. Delayed rod-mediated dark adaptation is a functional biomarker for incident early age-related macular degeneration. *Ophthalmology*. 2016;123:344–351.
92. Jackson GR, et al. Diagnostic sensitivity and specificity of dark adaptometry for detection of age-related macular degeneration. *Invest Ophthalmol Vis Sci*. 2014;55:1427–1431.
93. Nittala MG, et al. Retinal sensitivity using microperimetry in age-related macular degeneration in an Amish population. *Ophthalmic Surg Lasers Imaging Retina*. 2019;50:e236–e241.
94. Trinh M, Kalloniatis M, Nivison-Smith L. Radial peripapillary capillary plexus sparing and underlying retinal vascular impairment in intermediate age-related macular degeneration. *Invest Ophthalmol Vis Sci*. 2021;62:2.
95. Telias M, Nawy S, Kramer RH. Degeneration-dependent retinal remodeling: looking for the molecular trigger. *Front Neurosci*. 2020;14:1347.
96. Aplin FP, et al. Retinal changes in an ATP-induced model of retinal degeneration. *Front Neuroanat*. 2016;10:46.
97. Telias M, et al. Retinoic acid induces hyperactivity, and blocking its receptor unmasks light responses and augments vision in retinal degeneration. *Neuron*. 2019;102:574–586.e5.
98. Kauppinen A, Paterno JJ, Blasiak J, Salminen A, Kaarniranta K. Inflammation and its role in age-related macular degeneration. *Cell Mol Life Sci*. 2016;73:1765–1786.
99. Litwińska Z, et al. The interplay between systemic inflammatory factors and microRNAs in age-related macular degeneration. *Front Aging Neurosci*. 2019;11:286.
100. Ozaki E, et al. Inflammation in age-related macular degeneration. *Adv Exp Med Biol*. 2014;801:229–235.
101. Cheung CMG, Wong TY. Is age-related macular degeneration a manifestation of systemic disease? New prospects for early intervention and treatment. *J Intern Med*. 2014;276:140–153.
102. Büssow H. The astrocytes in the retina and optic nerve head of mammals: a special glia for the ganglion cell axons. *Cell Tissue Res*. 1980;206:367–378.

Investigative Ophthalmology & Visual Science